# The SN Ia runaway LP 398-9: detection of circumstellar material and surface rotation

Vedant Chandra [1,2]★ Hsiang-Chih Hwang [2,3] Nadia L. Zakamska [2,3] Simon Blouin [4,5]
Andrew Swan [6] Thomas R. Marsh [7] Ken J. Shen [8] Boris T. Gänsicke [7] J. J. Hermes [9]
Odelia Putterman [9] Evan B. Bauer [1] Evan Petrosky [2,10] Vikram S. Dhillon [11,12]
Stuart P. Littlefair [11] and Richard P. Ashley [7,13]

[1]*Center for Astrophysics | Harvard & Smithsonian, 60 Garden St, Cambridge, MA 02138, USA*
[2]*Department of Physics & Astronomy, Johns Hopkins University, 3400 N Charles St, Baltimore, MD 21218, USA*
[3]*Institute for Advanced Study, Einstein Drive, Princeton, NJ 08540, USA*
[4]*Los Alamos National Laboratory, PO Box 1663, Los Alamos, NM 87545, USA*
[5]*Department of Physics and Astronomy, University of Victoria, Victoria, BC V8W 2Y2, Canada*
[6]*Department of Physics & Astronomy, University College London, Gower Street, London WC1E 6BT, UK*
[7]*Department of Physics, University of Warwick, Coventry, CV4 7AL, UK*
[8]*Department of Astronomy and Theoretical Astrophysics Center, University of California, Berkeley, CA 94720, USA*
[9]*Department of Astronomy & Institute for Astrophysical Research, Boston University, 725 Commonwealth Ave., Boston, MA 02215, USA*
[10]*Department of Physics, University of Michigan, 450 Church St, Ann Arbor, MI 48109, USA*
[11]*Department of Physics and Astronomy, University of Sheffield, Sheffield S3 7RH, UK*
[12]*Instituto de Astrofísica de Canarias, E-38205 La Laguna, Tenerife, Spain*
[13]*Isaac Newton Group of Telescopes, Apartado de Correos 321, Santa Cruz de La Palma, E-38700, Spain*

## ABSTRACT

A promising progenitor scenario for Type Ia supernovae (SNeIa) is the thermonuclear detonation of a white dwarf in a close binary system with another white dwarf. After the primary star explodes, the surviving donor can be spontaneously released as a hypervelocity runaway. One such runaway donor candidate is LP 398-9, whose orbital trajectory traces back $\approx 10^5$ yr to a known supernova remnant. Here, we report the discovery of carbon-rich circumstellar material around LP 398-9, revealed by a strong infrared excess and analysed with follow-up spectroscopy. The circumstellar material is most plausibly composed of inflated layers from the star itself, mechanically and radioactively heated by the past companion's supernova. We also detect a 15.4 h periodic signal in the UV and optical light curves of LP 398-9, which we interpret as surface rotation. The rotation rate is consistent with theoretical predictions from this supernova mechanism, and the brightness variations could originate from surface inhomogeneity deposited by the supernova itself. Our observations strengthen the case for this double-degenerate SNIa progenitor channel, and motivate the search for more runaway SNIa donors.

**Key words:** circumstellar matter – stars: rotation – supernovae: general – white dwarfs.

## 1 INTRODUCTION

Type Ia supernovae (SNe Ia) are luminous transients that are valuable standard candles to measure cosmological parameters (e.g. Riess et al. 1998; Perlmutter et al. 1999; Riess et al. 2019), and play a crucial role in the chemical evolution of stellar populations (e.g. Tinsley 1979; Matteucci et al. 2009; Kirby et al. 2019). Despite the importance of SNeIa, their progenitor scenario is uncertain, and is the subject of intense theoretical and observational efforts (see e.g. Hillebrandt & Niemeyer 2000; Maoz, Mannucci & Nelemans 2014; Soker 2019, for a review). It is generally accepted that SNe Ia originate from massive white dwarfs (WDs) that accrete matter from

binary companions, but the nature and fate of the donor companion is unknown.

For several decades, the leading hypothesis was the 'single degenerate' scenario (e.g. Whelan & Iben 1973), in which a carbon–oxygen core (C/O) WD accretes matter from a non-degenerate star until it approaches the Chandrasekhar limit (Chandrasekhar 1931). However, it is challenging for the accreting WD to gain mass in the first place (e.g. Nomoto 1982; Iben & Tutukov 1984), and there is a growing body of observational evidence that suggests most SNe Ia cannot originate from single-degenerate progenitors (e.g. Kerzendorf et al. 2009; Kasen 2010; Li et al. 2011; Bloom et al. 2012; Margutti et al. 2012; Woods et al. 2017). An alternative is the 'double degenerate' scenario in which two WDs could either merge and consequently explode (e.g. Iben & Tutukov 1984; Webbink 1984), or have one WD detonate after mass transfer (e.g. Bildsten

★ E-mail: vedant.chandra@cfa.harvard.edu

et al. 2007). The explosion mechanism can be a double detonation, during which a detonation in the outer helium shell induces a second detonation in the carbon core that is powerful enough to unbind the star (Taam 1980; Guillochon et al. 2010; Dan et al. 2011; Raskin et al. 2012; Pakmor et al. 2013; Shen & Bildsten 2014).

In the double-degenerate case, a double detonation can occur during the mass transfer phase, well before the two WDs merge. In this 'dynamically driven double-degenerate double-detonation' ($D^6$) scenario, the primary WD can explode well below the Chandrasekhar limit (Pakmor et al. 2013; Shen et al. 2018a,b; Tanikawa, Nomoto & Nakasato 2018; Tanikawa et al. 2019). Observational studies have independently found that a significant fraction of SNeIa could originate from sub-Chandrasekhar mass WDs (Scalzo et al. 2014; Dhawan et al. 2017; Kirby et al. 2019; de los Reyes et al. 2020; Sanders, Belokurov & Man 2021). Recent theoretical work has shown that the $D^6$ mechanism can reproduce the observational signatures of most SNIa (Shen et al. 2021a,b). In this scenario, the donor WD could survive the explosion of the primary if it occurs in the early stages of mass transfer (Shen & Schwab 2017). The binary orbit becomes spontaneously unbound after the supernova, ejecting the donor WD at the orbital velocity, $\gtrsim 1000\,\mathrm{km\,s^{-1}}$.

Shen et al. (2018b) discovered three candidates that appear to be 'runaway' WD donors ejected from SNe Ia that exploded via the $D^6$ mechanism. These stars are among the fastest unbound stars in the Galaxy, with estimated space velocities $\gtrsim 1000\,\mathrm{km\,s^{-1}}$. Their radii are inflated by an order of magnitude compared to typical WDs, likely due to deposited energy from the SN Ia ejecta. These stars do not fit into any classical spectroscopic WD subtypes, due to their much lower apparent surface gravity and peculiar composition. All three candidates in Shen et al. (2018b) have similar low-resolution optical spectra, with absorption signatures of carbon, oxygen, magnesium, and calcium. One of these candidates is LP 398-9, referred to as 'D6-2' in Shen et al. (2018b). Remarkably, LP 398-9's inferred orbital trajectory extrapolated back $9 \times 10^4$ yr passes through the on-sky position of a known supernova remnant G70.0-21 (Fesen et al. 2015; Shen et al. 2018b; Raymond et al. 2020). G70.0-21 lies far off the Galactic plane, suggesting that it is a Type Ia remnant, and its shock velocity-inferred distance is $1 - 2$ kpc, consistent with LP 398-9's distance of $\approx 1$ kpc.

Here, we present follow-up observations of LP 398-9 that reveal the presence of significant quantities of circumstellar material, as well as a 15.4 h photometric period. We argue that both of these observables can be linked to the $D^6$ origin of the system, strengthening the case for this SNIa progenitor channel. After summarizing our data and observations in Section 2, we present our analysis in Section 3. We present our results in Section 4, and discuss our findings in Section 5.

## 2 DATA

In this section, we describe the archival data we collected for LP 398-9, as well as our own follow-up observations. In Section 2.1 we assemble the spectral energy distribution (SED) from archival data. In Section 2.2, we describe our light curves and follow-up photometry, and in Section 2.3, we describe our follow-up spectroscopy.

### 2.1 Spectral Energy Distribution

LP 398-9 has reliable archival photometry in the *GALEX NUV* (Martin et al. 2005; Million et al. 2016), Sloan *ugriz* (Fukugita et al. 1996; Gunn et al. 1998; Doi et al. 2010; Blanton et al. 2017; Ahumada et al. 2020), 2MASS *JH* (Skrutskie et al. 2006), and *WISE W1,W2*
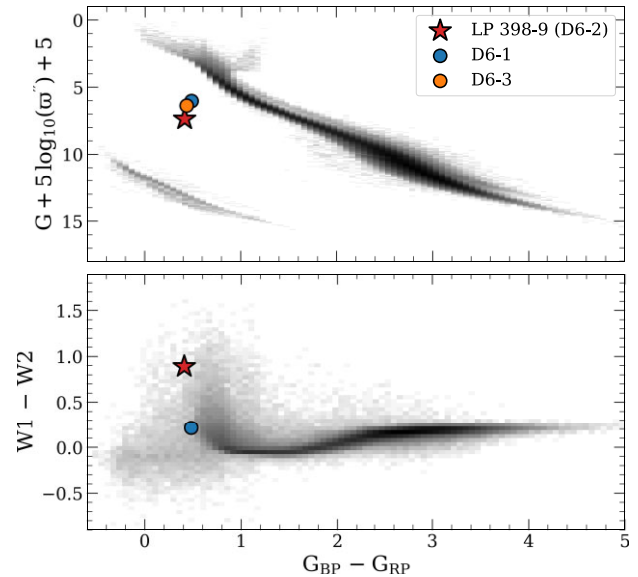


**Figure 1.** Top: location of LP 398-9 on the *Gaia* EDR3 colour-magnitude diagram. The background sample consists of stars within 100pc of the Sun (Gaia Collaboration et al. 2021). Bottom: the *Gaia-WISE* colour–colour space, with the same background sample of nearby stars. LP 398-9 has a significant excess in the *W1-W2* colour compared to other stars of a similar optical colour. For comparison, we show the other two $D^6$ candidates from Shen et al. (2018b). 'D6-3' does not have secure WISE photometry due to a crowded field, and is consequently absent from the bottom panel.

(Wright et al. 2010; Mainzer et al. 2011; Mainzer et al. 2014) bands. The detections in *GALEX FUV*, 2MASS *Ks*, and *WISE W3,W4* are unreliable or absent. LP 398-9 also has secure astrometry from the *Gaia* space observatory Early Data Release 3 (EDR3; Prusti et al. 2016; Mignard et al. 2018; Brown et al. 2021; Lindegren et al. 2021), with $\varpi/\sigma_\varpi \sim 18$. We correct the observed photometry for interstellar extinction along the line of sight using 3D dust maps (Green 2018; Green et al. 2015, 2018b,a) queried at the *Gaia* inverse-parallax distance of 840 pc. We adopt the extinction law of Fitzpatrick & Massa (2007) with $R_V = 3.1$. The *Gaia* colour–magnitude diagram and *Gaia–WISE* colour–colour diagram of LP 398-9 are shown in Fig. 1. The lower panel shows LP 398-9's infrared excess compared to other stars at a similar optical colour. Of the other two $D^6$ candidates from Shen et al. (2018b), D6-1 has no $W1 - W2$ colour excess, and D6-3 is in a crowded field and consequently does not have secure *WISE* photometry.

One potential contaminant of *WISE* imaging is source confusion due to the relatively coarse angular resolution of *WISE* (see e.g. Dennihy et al. 2020). In Fig. 2, we compare the *J*-band image from 2MASS to the AllWISE image in channel *W1*. In the 2MASS image, there is no discernible background source within 6 arcseconds of LP 398-9. Furthermore, because the *WISE* data of LP 398-9 appears time-variable (Section 3.3), we exclude the possibility of a background blazar by finding no radio counterpart in the NRAO VLA Sky Survey (NVSS; Condon et al. 1998). A conclusive method to verify the association between the *WISE* data and LP 398-9 is by comparing optical astrometry to the source position measured by *WISE*. In Fig. 2, we display time-averaged measurements of the position of LP 398-9 on the sky as measured over 5 yr of the NEOWISE mission (2014–2019), along with the reference position from AllWISE in 2011 (Cutri et al. 2012). We perform a trimmed least-squares linear regression (Rousseeuw & Van Driessen 2006;
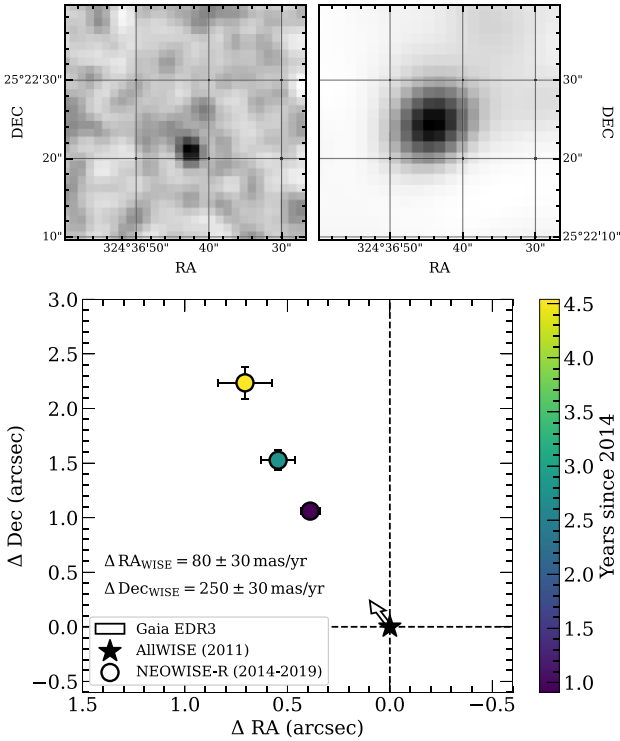
**Figure 2.** Top left: 2MASS *J* band image from ≈2001. Top right: AllWISE channel *W1* image ten years later, from ≈2011. The centroid has clearly shifted by several arcseconds towards the NE direction. Bottom: position of LP 398-9 on the sky during the course of 5 yr of the NEOWISE mission. Each data point is the average of 20 individual measurements. The arrow indicates 1 yr of the *Gaia* EDR3 proper motion, centred on the AllWISE coordinate. There is no bright contaminant within 6 arcseconds and the *WISE* proper motion is consistent with the optical proper motion from *Gaia*, supporting the fact that the IR excess and variability comes from LP 398-9 itself.

Cappellari et al. 2013) on the RA and Dec as a function of time to estimate the *WISE* proper motion. The parallax motion of ∼1 mas (known from *Gaia*) is negligible here. We obtain $\Delta RA_{WISE} = 80 \pm 30$ mas yr$^{-1}$ and $\Delta Dec_{WISE} = 250 \pm 30$ mas yr$^{-1}$. This is consistent within 1-$\sigma$ with the *Gaia* EDR3 proper motion of LP 398-9 (Table 1). To ensure our method is robust, we compute the *WISE* proper motions of some nearby objects in the field and verify that they too match their *Gaia* data within uncertainties. This astrometric test confirms that the *WISE* photometric source is securely associated with LP 398-9.

## 2.2 Light curves

In addition to the time-averaged catalog measurements from All-WISE, we utilize individual exposures taken over the past nine years. We assemble the *WISE* light curve of LP 398-9 by querying the AllWISE (Wright et al. 2010) and NEOWISE (Mainzer et al. 2011; Mainzer et al. 2014) databases for single-exposure photometric measurements. There are 27 AllWISE data points from 2010 May 27 to 2010 November 10, and 178 NEOWISE data points from 2014 May 31 to 2019 November 10. We perform quality cuts to remove spurious detections with outlying RA/Dec offsets and undefined magnitude uncertainties. The resulting light curve has 168 data points over a 9 yr baseline. The cadence of the observations is irregular and follows the *WISE* position-dependent scanning strategy,

**Table 1.** Parameters of LP 398-9.

| Parameter | Value |
|---|---|
| Gaia EDR3 | |
| Source ID | 1798008584396457088 |
| RA (degrees) | 324.61250 |
| Dec. (degrees) | 25.37374 |
| G (mag) | 16.97 |
| BP−RP (mag) | 0.41 |
| $\varpi$ (mas) | $1.19 \pm 0.06$ |
| Distance (pc) | $840 \pm 40$ |
| $\mu_{RA}$ (mas yr$^{-1}$) | $98.28 \pm 0.07$ |
| $\mu_{DEC}$ (mas yr$^{-1}$) | $240.18 \pm 0.06$ |
| $v_T$ (km s$^{-1}$) | $1010 \pm 60$ |
| Stellar model | |
| $T_{eff}$ (K) | $7500 \pm 100$ |
| Radius (R$_\odot$) | $0.20 \pm 0.01$ |
| Mass (M$_\odot$) | U [0.2, 0.8] (assumed) |
| $\log\left[g, \mathrm{cm\,s^{-2}}\right]$ | $5.5 \pm 0.2$ |
| $v_R$ (km s$^{-1}$) | $80 \pm 10$ |
| Blackbody infrared model | |
| $T_{bb}$ (K) | $670 \pm 50$ |
| $R_{bb}$ (R$_\odot$) | $5.4 \pm 0.9$ |
| $M_{dust}$ (g) | $\sim 10^{20}$ |
| Flat disc infrared model ($i = 0°$) | |
| $T_{in}$ (K) | $1300 \pm 200$ |
| $T_{out}$ (K) | $\approx 300$ |

with a ≃ 180 d gap between successive observing runs. Each run is ≈1.5 d long and consists of exposures taken ≈1.5 h apart.

We queried archival photometry for LP 398-9 from the Zwicky Transient Facility (ZTF; Bellm et al. 2019; Masci et al. 2019). We assembled a light curve consisting of data points collected between 2020 January 13 and 2021 April 27 in the *g* and *r* photometric bands. We only used the most recent year of ZTF data to minimize the effect of long term brightness variations (discussed further in Section 3.3). To maximize our time coverage, we combined the *g* and *r* data after subtracting their respective median magnitudes (e.g. Burdge et al. 2020). We removed bad data points with ZTF quality flag `catflags > 0` and sharpness `sharp > 0.5` (e.g. Guidry et al. 2021). Our final ZTF *gr* lightcurve has 205 data points.

We observed LP 398-9 with HiPERCAM (Dhillon et al. 2016, 2018; Dhillon et al. 2021) on the 10.4-m Gran Telescopio Canarias (GTC) at the Observatorio del Roque de los Muchachos on the island of La Palma, Spain, on 2018 June 11 from 03:38 to 05:15 UTC (PI: Dhillon). We utilized a customised high-throughput approximation of the Sloan *ugriz* filter set to obtain simultaneous 5-band photometry. A cadence of 1.222 sec was used for the *g*, *r* and *i* arms, while every other readout was skipped on the *u* and *z* arms giving a 2.444 sec cadence. The weather was clear with seeing ∼ 0.8″–1.5″. The Moon was 80 per cent illuminated. We debiased and flat-fielded the data using twilight sky flats. We performed comparative aperture photometry using apertures that tracked the target positions with radii set to 1.8 times the mean full width at half-maximum of the stellar profiles. We defer to Dhillon et al. (2021) for further details of the reduction procedures. We used *Gaia* EDR3 1798008691771518464 (*G* = 15.1) as the main comparison star, and *Gaia* EDR3 1798020408442309248 (*G* = 16.5) to confirm that the main comparison star was not itself variable. We also observed LP 398-9 with the Wide Field Camera on the 2.5-m Isaac Newton Telescope (INT), on 2018 August 2 from 00:17 to 04:44 UTC. We utilized a Sloan *g* filter with exposure times of 100 sec. We performed aperture photometry relative to a

comparison star, and defer to Dhillon et al. (2021) for further details on the reduction procedures.

We observed LP 398-9 with the IO:O imager on the 2-m Liverpool Telescope (LT; Steele et al. 2004) at the Observatorio del Roque de los Muchachos, over the course of a month from 2021 July 8 to 2021 August 8 (PI: Gänsicke). We obtained a total of 154 images in the Bessel *B* band (effective wavelength $\simeq 4450$ Å) with an exposure time of 60 s, averaging approximately five images per night. We performed comparative aperture photometry against the nearby star *Gaia* EDR3 1798008721834715648 ($G = 13.8$).

We also analyse observations of LP 398-9 obtained with the Space Telescope Imaging Spectrograph (STIS; Woodgate et al. 1998) of the *Hubble Space Telescope* (*HST*) over six consecutive orbits on 2020 October 3 (PI: Shen). The spectra are flux-calibrated and cover a wavelength range of 1600–3600 Å with the G230L grating. We use these spectra to derive an ultraviolet light curve that is analysed in this paper. A full analysis of the STIS spectrum will be presented in a forthcoming publication. We took advantage of the photon-counting `TIME-TAG` mode to re-bin the spectra into 9-min exposure times, and computed the average flux in the 1700–3100 Å range (e.g. Hermes et al. 2021). The resulting light curve has an effective central wavelength of 2520 Å, and contains 28 data points over $\approx 8$ continuous hours.

## 2.3 Spectroscopy

Shen et al. (2018b) obtained a low-resolution spectrum ($R \approx 300$) of LP 398-9 from 3400 – 9000 Å with the Nordic Optical Telescope (NOT). They noted absorption lines indicating the presence of carbon, oxygen, magnesium, and calcium in the stellar photosphere, and measured a radial velocity $20 \pm 60$ km s$^{-1}$.

We obtained a mid-resolution spectrum of LP 398-9 on 2020 November 14 using the Dual-Imaging Spectrograph (DIS) on the 3.5-m telescope at the Apache Point Observatory (PI: Chandra). We employed the B1200/R1200 gratings and a 1.5 arcsec slit width, providing a spectral resolution (Gaussian $\sigma$) of 2 Å on the blue end and 0.5 Å on the red end, as estimated with sky emission lines. We obtained four 10-min exposures bracketed by arc lamp exposures to ensure a reliable wavelength calibration. Our data covered a wavelength range of 4000–7000 Å, with a dichroic gap between 5200–6000 Å. We performed a standard data reduction—bias correction, flat-fielding, aperture extraction, and wavelength calibration—using the pipeline tools in IRAF (Tody 1986).

We compared the O I absorption line at $\lambda 7002.23$ Å with its theoretical rest wavelength to derive a radial velocity $80 \pm 10$ km s$^{-1}$, which is consistent with the earlier measurement made by Shen et al. (2018b). We also used the $\lambda 6300$ Å O I sky emission line to verify that our absolute wavelength calibration is accurate to within 5 km s$^{-1}$. We therefore do not detect radial velocity variations that would indicate the presence of a close binary companion. As noted by Shen et al. (2018b), the low radial velocity is somewhat unexpected considering LP 398-9's hypervelocity space motion, but could be a statistical fluctuation due to small numbers and selection effects.

## 3 ANALYSIS

In this section, we analyse our spectro-photometric observations of LP 398-9. We confirm the hypervelocity nature of LP 398-9 with the latest data from Gaia (Section 3.1). We model the SED of LP 398-9 and its excess infrared emission to derive the system's parameters (Section 3.2). We present multi-band light curves that exhibit a 15.4 h period, which we interpret as surface rotation (Section 3.3).

Finally, we present follow-up spectroscopy that reveals the presence of circumstellar carbon (Section 3.4).

### 3.1 Hypervelocity

We confirm the hypervelocity status of LP 398-9 using newly released astrometric data from Gaia EDR3 (Brown et al. 2021; Lindegren et al. 2021; Lindegren et al. 2021). LP 398-9 is among the highest tangential velocity stars in the *Gaia* data set. Furthermore, it is the sole 15-sigma outlier in the tangential velocity distribution of stars within seven degrees of the SN remnant G70.0-21. Previously, Shen et al. (2018b) used data from Gaia DR2 to find a 99 per cent credible interval of $v_T = [700, 1500]$ km s$^{-1}$ for the tangential proper motion velocity of LP 398-9. The EDR3 parallax is nearly twice as precise as DR2, and the proper motions are more precise by a factor of four. We use the affine-invariant Markov Chain Monte Carlo (MCMC) sampler `emcee` (Foreman-Mackey et al. 2013; Foreman-Mackey et al. 2019) to sample the new astrometric data from Gaia EDR3 and consequently derive an updated posterior distribution for $v_T$. We include all covariances and perform a zero-point correction to the parallax following Lindegren et al. (2021). We employ the exponentially decreasing space density prior described in Bailer–Jones (2015), although its effect is likely minimal since the EDR3 parallax is quite precise ($\varpi/\sigma_\varpi \sim 18$). We find a median tangential velocity $v_T = 1010 \pm 60$ km s$^{-1}$, with a 99 per cent credible interval of $v_T = [890, 1150]$ km s$^{-1}$. The implied total Galactocentric velocity (including our radial velocity measurement from Section 2.3) is $v_{Gal} = 1130 \pm 60$ km s$^{-1}$. This secures LP 398-9's status as a hypervelocity star, despite its low apparent radial velocity. The broad conclusions from Shen et al. (2018b) about LP 398-9's Galactic trajectory are unchanged.

### 3.2 SED model and IR excess

To investigate the infrared excess of LP 398-9, we first fit a stellar model to the observed photometry at optical wavelengths, and then compare the predicted stellar flux in the infrared to the observed IR photometry. We fit the SED of LP 398-9 in the SDSS *ugriz* passbands using a bespoke grid of model spectra computed with the atmosphere code described in Blouin, Dufour & Allard (2018a), Blouin et al. (2018b). Since the non-detection of hydrogen lines in the spectrum of LP 398-9 rules out the presence of atmospheric hydrogen, we assume a helium-dominated atmosphere. The SED can also be altered by the presence of metals due to line blanketing and changes in the atmospheric opacity. We therefore use the NOT spectrum of LP 398-9 observed by Shen et al. (2018b) to set the metallicity to [Ca/He] = -11.2, with other abundances scaled to solar proportions. We adopt a surface gravity $\log g = 5.5$ when computing the model spectra, and verify that neither the photometric nor spectroscopic fits are very sensitive to the assumed metallicity and surface gravity.

We assume flat priors on the stellar parameters: $2500 \leq T_{eff}/K \leq 10\,000$ and $0.05 \leq R/R_\odot \leq 1$. We adopt a Gaussian prior on the parallax $\varpi/$mas with a mean and standard deviation defined by the *Gaia* EDR3 astrometric measurement $\pi = 1.19 \pm 0.06$ mas. To prevent any single band with underestimated uncertainties from dominating the fit, we implement a floor uncertainty of 0.03 magnitudes in all bands (e.g. Bergeron et al. 2019). We define a log-likelihood (the $\chi^2$ statistic multiplied by $-0.5$) to compare the model fluxes to the observed fluxes and perform a preliminary fitting step to estimate the atmospheric parameters of LP 398-9. We maximize the photometric likelihood over the stellar parameters ($T_{eff}$ and $R$). Next, using the preliminary stellar parameters as initial

values, we sample the posterior distributions of $T_{eff}$, $R$, and $\varpi$ using `emcee`. The stellar parameters are summarized in Table 1, along with uncertainties computed by taking the standard deviation of the respective MCMC samples. We adopt the posterior sample with the highest log-likelihood as our best-fitting stellar parameters for LP 398-9: $T_{eff} = 7500 \pm 100$ K, $R = 0.20 \pm 0.01\,R_\odot$.

We repeated our analysis assuming oxygen-dominated and carbon-dominated atmospheres. The inferred $T_{eff}$ and $R$ are similar for the helium and oxygen atmospheres. A carbon-dominated atmosphere is ruled out, since it would require the presence of strong molecular $C_2$ absorption lines that are absent in our spectroscopic observations (discussed further in Section 3.4). The mass of LP 398-9 is quite uncertain, since the stellar structure is unknown and the star is in a temporarily inflated state. However, given the $D^6$ origin of the system, the mass could plausibly lie in the 0.2–0.8 $M_\odot$ range (Shen 2015; Shen et al. 2018b), with the runaway velocity suggesting a mass on the lower end (Bauer et al. 2021). Assuming a uniform mass prior in this range, our fitted photometric radius implies $\log g \approx 5.5 \pm 0.2$. This is consistent with the Ca II H and K absorption lines on the archival NOT spectrum.

To quantify and model the infrared excess around LP 398-9 we use the AllWISE catalog magnitudes in the *W1* and *W2* channels. We convert them to fluxes, and subtract the expected flux of LP 398-9 at these wavelengths using the stellar model described above. To this excess flux, we fit two models: a blackbody, and a flat disc model. The blackbody is parametrized by the temperature $T_{bb}$ and a normalization factor that depends on the solid angle subtended on the sky. We use the *Gaia* EDR3 parallax of LP 398-9 to fix its distance, fitting for the remaining normalization radius $R_{bb}$ in addition to $T_{bb}$.

For the disc model, we use the geometrically thin, optically thick debris disc model of Jura (2003). With a known distance, this model is further constrained by the stellar temperature $T_{eff}$ and radius $R$, with the free parameters being the two temperatures corresponding to the inner edge ($T_{in}$) and outer edge ($T_{out}$) of the disc. The inclination of the disc is difficult to constrain with the available observations, although it is probably low (more face-on) given the brightness of the IR excess compared to the star. Additionally, the temperature of the outer edge of the disc $T_{out}$ is poorly constrained because observations at longer wavelengths are not available.

We fit the respective models using the nonlinear minimization algorithms in `scipy.optimize` (Virtanen et al. 2020). We repeat the fit on $10^4$ Monte Carlo replicates of the data (adding the relevant Gaussian errors to the observed fluxes) to estimate the uncertainties on the parameters. The pure stellar, stellar + blackbody, and stellar + flat disc models are illustrated with the observed SED in Fig. 3, and the best-fit IR model parameters are summarized in Table 1.

The blackbody temperature can be interpreted as the average temperature of an inflated, optically thin dust shell (Xu et al. 2018). Given the low temperature $T_{bb} \approx 670$ K and large normalization radius $R_{bb} \approx 5.4\,R_\odot$, we can rule out stellar or sub-stellar companions. A brown dwarf with $T_{eff} \sim 700$ K would have a radius $\sim 0.1\,R_\odot$ (e.g. Sorahana, Yamamura & Murakami 2013), almost fifty times smaller than the radius we derive from the normalization of the IR excess. Depending on the typical grain sizes, $T_{bb} \approx 670$ K corresponds to dust located at orbital radii $\approx 10$–$30\,R_\odot$, or around 50–150 times the present radius of the star (Xu et al. 2018).

The flat disc model does not match the observed fluxes well, indicating that a geometrically thin, optically thick disc is insufficient to describe the material around LP 398-9. A low inclination ($\approx 0°$ – $30°$) provides the best match to the *W1* and *W2* data. The inclination and inner disc temperature are degenerate – assumed inclinations of [0°, 30°, 60°] result in best-fitting $T_{in} \approx$ [1300,
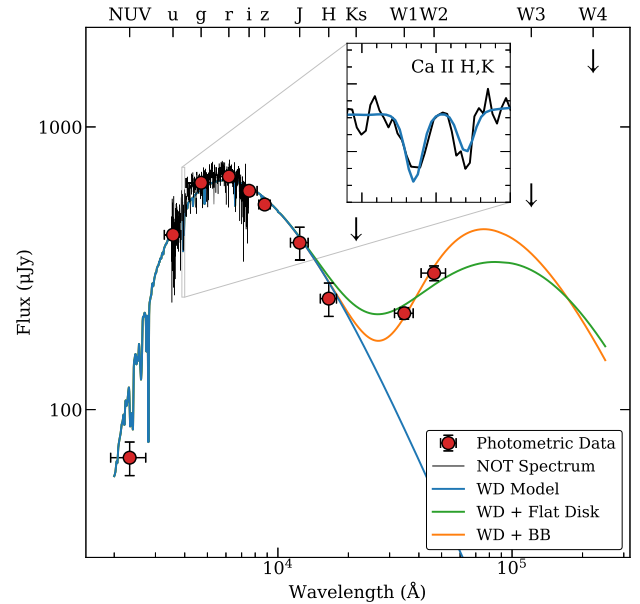


**Figure 3.** SED of LP 398-9 with our best-fitting model for the WD and IR excess. The observed photometric bands are indicated on the top axis. The inset shows the 3890–4000 Å region of the archival NOT spectrum, with the best-fitting stellar model spectrum overlaid. Downward arrows indicate upper limits. Uncertainties are 1-sigma after applying our 0.03 mag floor, and in some cases are smaller than the marker size.

1600, 2000] K. Depending on the size and composition of the grains, circumstellar dust sublimates at temperatures between 1200–2000 K, and consequently any material inwards of the radius corresponding to $T_{in}$ rapidly sublimates away, leaving a gap between the star and the debris disc (von Hippel et al. 2007; Rafikov & Garmilla 2012; Xu et al. 2018). Therefore, the inferred inner temperature $T_{in} \approx 1300$ K is broadly consistent with dust sublimation temperatures, although the flat disc geometry seems unlikely. Our favored interpretation is a circumstellar dust shell model with a characteristic temperature of $T_{bb} \approx 670$ K.

### 3.3 Periodic photometric variability

We searched the LT photometry of LP 398-9 for periodic variations using a Lomb–Scargle periodogram (Lomb 1976; Scargle 1982). We find a dominant peak at $f = 1.55$ d$^{-1}$, corresponding to a period of $\approx 15.4$ h. We repeat our periodogram analysis on the ZTF photometry. Fitting the entire ZTF baseline from 2018 April 20 to 2021 April 27 yields a period 1 per cent smaller than the LT period. However, this ZTF light curve has significant long-term brightness variations that contaminate the periodogram, requiring pre-whitening to remove trends. If we instead fit only the most recent ZTF campaign from 2020 January 6 to 2021 April 27 without pre-whitening, we derive a period within 0.03 per cent of the LT period. We therefore use only the ZTF data from 2020 January 6 onwards in our subsequent analysis.

We adopt the peak of the LT periodogram as our assumed period. To estimate the uncertainty of this measurement, we computed 2500 Monte Carlo replicates of the LT light curve by adding Gaussian uncertainties, and computed half the difference between the 84th and 16th quantiles of the resulting period distribution. We derive a best-fit period $P = 15.441 \pm 0.016$ hr. We phase-fold the STIS, LT, and ZTF light curves and display them in Fig. 4. We fit a sinusoidal
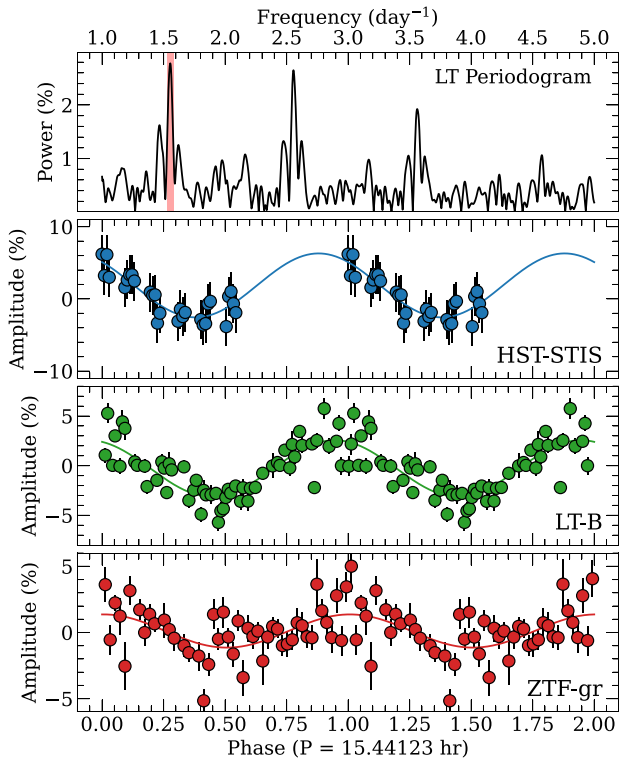
**Figure 4.** Lomb–Scargle periodogram of the LT light curve of LP 398-9, along with the phase-folded *HST*-STIS, LT-*B*, and ZTF-*gr* light curves. The STIS data points are unbinned and consecutive from a single epoch, while the LT and ZTF data points are binned in phase. We overlay the sinusoidal models used to estimate the variability amplitude of each light curve.

model to each phase-folded (un-binned) light curve to estimate the variability amplitudes. We find amplitudes of $4.4 \pm 0.6$ per cent for STIS, $2.8 \pm 0.2$ per cent for LT-*B*, and $1.3 \pm 0.3$ per cent for ZTF-*gr*. Fig. 4 shows a slight colour-dependent phase difference between the three data sets. However, simply changing the assumed period by as little as 0.3 per cent (to $P = 15.40317$, for example) can erase this apparent phase difference. Therefore, the most plausible explanation is that this phase difference is non-physical, and is simply an artefact of systematic uncertainties in our photometry and period measurement.

Our 100-min HiPERCAM *ugriz* observations are illustrated in Fig. 5. The time baseline of this observation covers a fraction of our derived rotational period, and therefore represents a quasi-linear segment of the rotationally modulated flux variation. Both our HiPERCAM-*ugriz* and subsequent INT-*g* observations (not shown here) caught LP 398-9 in the dimming phase. We quantify the colour dependence of the flux decline by fitting a simple linear regression to the light curves in each band using the trimmed least squares approach described in Cappellari et al. (2013). The rate of decline (slope) is strongly wavelength-dependent, with the bluest photometry declining twice as quickly as the reddest. The *g*-band slope is identical within uncertainties between the HiPERCAM and INT data. The trend of the HiPERCAM colour-dependence (blue declining faster than red) is consistent with the trend in the variability amplitudes of the STIS, LT-*B*, and ZTF-*gr* light curves.

The colour-dependence of the photometric variability could have several plausible explanations. A convective star-spot with a temperature lower than the surrounding photosphere could produce such
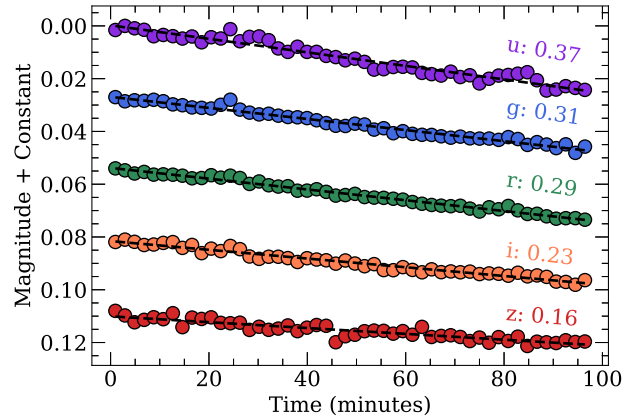


**Figure 5.** 100-min HiPERCAM light curve of LP 398-9. The *ugriz* bands are arranged from top to bottom. We overlay a linear fit to each data set with a black dashed line. The colour-dependent trend is visually discernible, with the bluest *u* band declining twice as fast as the reddest *z* band. For each band we show the fitted slope of the flux decline in magnitudes per day.

a signal, although it is challenging to constrain the temperature and size of the spot (e.g. Pelisoli et al. 2021). Alternatively, if a portion of the stellar surface is polluted with metals, there could be an opacity or line blanketing contrast as the star rotates. Additionally, light filtering through the circumstellar dust could be reddened by extinction.

As described in Section 2.1, we compiled a *WISE* light curve of LP 398-9 spanning 9 yr, grouped into 14 approximately day-long observing runs spaced 180 d apart. Phase-folding the *WISE* light curve to the inferred stellar rotation period of 15.4 h does not produce any coherent signal. This is expected, since the IR flux is dominated by emission from the surrounding circumstellar dust, which would greatly dilute any photometric variability from the star itself. However, the *WISE* data of LP 398-9 is overall more variable than the photometric uncertainties would indicate. We average the measurements in each observing run and illustrate the long-term *W1* and *W2* fluxes along with the *W1−W2* colour in Fig. 6. There is significant variation in both the *W1* and *W2* fluxes. The *W1−W2* colour marginally varies as well, potentially indicating a varying surface area or temperature of the circumstellar material. Recent evidence has shown that many WDs with debris discs are IR-variable (Swan, Farihi & Wilson 2019; Swan et al. 2020). Those systems are thought to exhibit stochastic variation over long time-scales due to collisional dust production and depletion (e.g. Kenyon & Bromley 2017b,a; Swan et al. 2021).

### 3.4 Spectroscopic evidence of circumstellar carbon

In Fig. 7 we illustrate the APO spectrum of LP 398-9, with several identified absorption lines of carbon, oxygen, magnesium, and calcium highlighted. We characterize the spectrum using theoretical models described in Blouin et al. (2018a,b). We adopt the convention that [X/He] denotes the logarithm of the number density ratio between species X and He. We fix the stellar parameters to the values computed from the SED fit in Section 3.2 and compute single-abundance spectra over a range of C and O to investigate the atmospheric composition We overlay in red a model spectrum with [C/He] $= -5.0$, and in blue a model with [O/He] $= -1.0$. The short-wavelength end of the spectrum demonstrates that this carbon abundance is already pushing the higher plausible limit, due to the development of strong $C_2$ bands that are absent from our observed
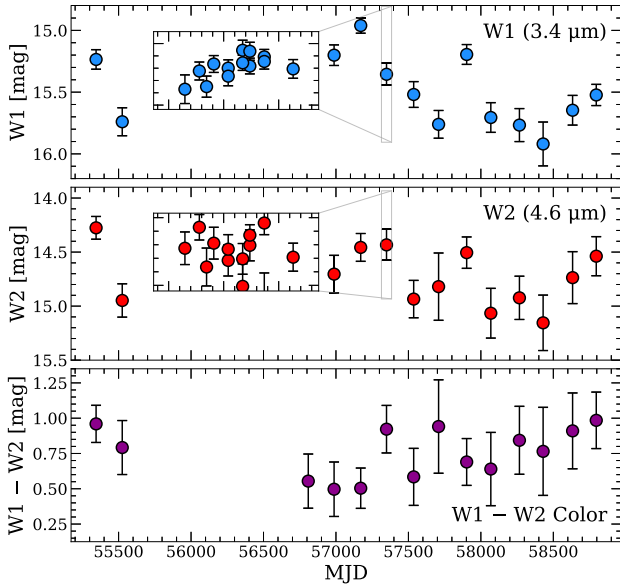
**Figure 6.** Long-term light curves from the duration of the *WISE* mission in the *W1* and *W2* bands, along with their difference. We average the individual measurements from each observing run to produce these data points. The insets show individual measurements from a single *WISE* observing run. The insets vertically span 1 magnitude, and horizontally span 2 d.
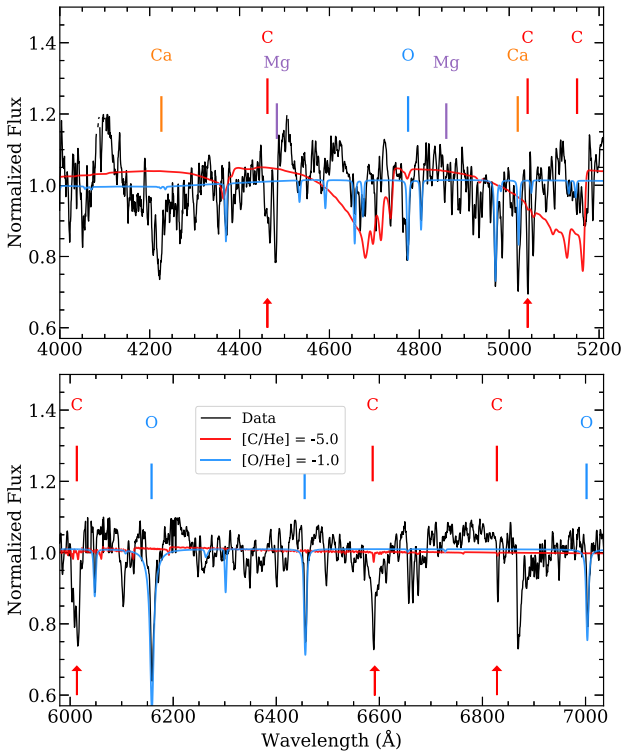


**Figure 7.** Mid-resolution spectrum of LP 398-9 from the 3.5-m telescope at the Apache Point Observatory, split into two wavelength regions. The spectrum is smoothed with a 3 Å boxcar. We indicate identified absorption lines of carbon, oxygen, magnesium, and calcium. We overlay in red a theoretical spectrum with the same stellar parameters as LP 398-9 and an atmospheric carbon abundance of [C/He] = -5.0, and independently in blue an oxygen abundance of [O/He] = -1.0. Red arrows indicate carbon absorption lines that cannot be explained by the stellar model, suggesting that they are formed in circumstellar material instead.

spectrum (Swan 1857; Johnson 1927). Yet, several narrow carbon lines remain unexplained by the stellar models (red arrows in Fig. 7).

The most plausible explanation for this non-photospheric absorption is the presence of circumstellar carbon gas around LP 398-9. Compared to the stellar photosphere, the circumstellar region has much lower pressures, and consequently contains less molecular $C_2$. This means more atomic C can be present to produce narrow absorption lines without creating large molecular bands on the spectrum. The two most prominent atomic carbon features are C I lines at 6587.6 Å and 6828.2 Å respectively. Based on their equivalent widths — 1.9 Å and 0.6 Å respectively — we can infer a column density of $\sim 10^{14}$ cm$^{-2}$ in the optically thin limit (Johansson 1966; Luo & Pradhan 1989; Hibbert et al. 1993; Draine 2011; Kramida et al. 2021). For comparison, this estimate is between one and two orders of magnitude lower than neutral carbon column densities around typical mass-losing asymptotic giant branch stars (e.g. Keene et al. 1993; Hasegawa & Kwok 2003). If the gas is co-spatial with the dust and occupies a region of order $R_{bb}$ from Section 3.2, then the implied gas mass would be similar to the inferred dust mass. Our present data do not constrain the spatial extent or geometric configuration of the gas and dust. We cannot rule out that a larger reservoir of dust surrounds LP 398-9, with only the material close to the star being heated and revealed by our observations of the IR excess and C I absorption.

Although we only report the detection of circumstellar carbon with our current data, future spectroscopy at higher resolution and higher signal-to-noise could reveal absorption from other species. We emphasize that the carbon and oxygen abundances stated in Fig. 7 are qualitative approximations used to investigate the presence of circumstellar absorption. A more sophisticated stellar model is required to separate the photospheric and circumstellar contributions to the spectrum, and enable a detailed abundance analysis of both components.

## 4 RESULTS

### 4.1 Photometric period

LP 398-9 exhibits sinusoidal photometric variation with a period $P \approx 15.4$ hr. A stellar companion is quite unlikely, given the non-detection of radial velocity variations $\gtrsim 10$ km s$^{-1}$. The most natural explanation is that this photometric period corresponds to the rotational period of the star (e.g. Brinkworth et al. 2005; Hermes et al. 2021). There are several possible mechanisms that can produce rotationally modulated variability. WDs with exceptionally strong magnetic fields can have continuum opacity variations on their surfaces, producing photometric variations at the rotational period (e.g. Ferrario et al. 1997; Tremblay et al. 2015). However, the optical spectrum of LP 398-9 does not indicate a strong magnetic field, given the absence of visible Zeeman splitting. An alternative possibility is the formation of weakly magnetized starspots in the convective envelope of the star (e.g. Brinkworth et al. 2004; Gänsicke et al. 2020). These spots would be cooler than the surrounding regions, producing chromatic variations in the observed flux as they rotated in and out of view (e.g. Kilic et al. 2015; Reding et al. 2020).

Another interesting possibility is that the surface inhomogeneity of LP 398-9 is related to its origin as a D$^6$ SN Ia donor. When its companion exploded $\sim 10^5$ yr ago, LP 398-9 would have been blasted by a wave of ejecta. These radioactive ejecta would have been asymmetrically deposited on the surface of LP 398-9 (e.g. Bauer, White & Bildsten 2019). In regular WDs, horizontal mixing can homogenize the surface distribution of pollutants on time-scales

of $10^1 - 10^6$ yr depending on the temperature and atmospheric composition (Cunningham et al. 2021). Since the stellar structure of LP 398-9 is quite uncertain, it is difficult to estimate the time-scale with which diffusion is expected to homogenize the stellar surface. The vertical diffusion time-scale is certainly long compared to regular WDs, since LP 398-9 is inflated to $\approx 10$ times the typical WD radius. If the deposited surface asymmetry does survive to the present day, then it could produce variable line blanketing and continuum opacity, possibly producing the observed photometric signal (e.g. Brinkworth et al. 2004; Kilic et al. 2015; Maoz, Mazeh & McQuillan 2015). If the surface abundances vary along the line of sight, this may be detectable with future time-resolved optical spectra.

Apart from the origin of the surface inhomogeneity, the rotational period of LP 398-9 can also be linked to the $D^6$ mechanism. Immediately prior to the SN explosion of the massive companion, the binary system would have been in an extremely compact, mass-transferring stage. The orbital velocity $v_{orb}$ of the donor (mass $M_2$) around the accreting primary (mass $M_1$) is given by

$$v_{orb}^2 = \frac{GM_1}{a(1 + M_2/M_1)} \,, \tag{1}$$

where $a$ is the orbital separation. LP 398-9 would have been ejected from the binary at $v_{orb}$ when its companion exploded. The amount of low-velocity material left behind by the exploded companion is negligible, so LP 398-9 has probably not slowed down much since the supernova. This allows us to express the orbital period in terms of the measured space velocity as

$$P_{orb} = \frac{2\pi a}{(1 + M_2/M_1)\, v_{orb}} = \frac{2\pi G M_1}{(1 + M_2/M_1)^2 v_{orb}^3} \,. \tag{2}$$

Assuming that the primary star that exploded as an SN is $\approx 1.0\,M_\odot$, and that the donor mass is somewhere in the range $M_2 = 0.2$–$0.8\,M_\odot$, this gives orbital periods at the time of SN detonation around $P_{orb} = 3$–$7$ min, based on the $\approx 1100$ km s$^{-1}$ space velocity of LP 398-9.

Although the tidal quality factor of WDs is uncertain, it is reasonable to expect a degree of tidal synchronization between the spin and orbit of the WDs (e.g. Iben, Tutukov & Fedorova 1998; Fuller & Lai 2011, 2012a,b, 2014; Yu, Weinberg & Fuller 2020; Yu, Fuller & Burdge 2021). There are a handful of known tidally-distorted WDs in compact binaries, and the non-detection of significant tidal heating could imply that synchronization is near-perfect (Benacquista 2011; Piro 2011). Under the assumption that tidal locking keeps $P_{rot} \approx P_{orb}$, our reasoning implies a rotation period $\approx 3$–$7$ min when the companion exploded. If LP 398-9 subsequently conserved its angular momentum, then the initial post-SN rotational period $P_i$ and radius $R_i$ and present-day $P_f$, $R_f$ can be related with

$$\frac{P_f}{P_i} = \left(\frac{R_f}{R_i}\right)^2 . \tag{3}$$

We can set $R_i \approx 0.01$–$0.02\,R_\odot$ using the mass-radius relation for $0.2$–$0.8\,M_\odot$ WDs, and set $R_f = 0.20\,R_\odot$ from our SED fit in Section 3.2. Applying equation (3), post-SN rotational periods $P_i \approx 3$–$7$ min correspond to present-day rotational periods $P_f \approx 5$–$50$ h, which brackets our observed photometric period of $15.4$ h for LP 398-9 (Section 2.2). A larger initial donor radius (e.g. due to heating during mass transfer) corresponds to a shorter present-day rotational period. Conversely, angular momentum was probably not entirely conserved. Additional effects like magnetic braking and mass loss could have further slowed the rotational rate of the system over time. These rough estimates demonstrate that the observed rotational period can be plausibly linked to the $D^6$ scenario, assuming LP 398-9 mostly conserved its angular momentum after the SN Ia explosion.

We emphasize here the differences and similarities between LP 398-9 and GD 492, another runaway star that was recently found to rotate with an 8.9 h period (Hermes et al. 2021). GD 492 has a peculiar composition that suggests it is the partially burnt accretor left over from a Type Iax supernova (Vennes et al. 2017; Raddi et al. 2018b,a, 2019). GD 492 also has a lower space velocity $\simeq 850$ km s$^{-1}$, implying that its donor companion was an He-burning subdwarf rather than another white dwarf (Bauer et al. 2019). In this scenario, GD 492 is rotating too slowly to be the runaway subdwarf donor, and is most likely the burnt remnant of the accreting primary that underwent a failed supernova. Conversely, the higher space velocity of LP 398-9 — and its remarkable spectroscopic similarity to two other $D^6$ systems with space velocities $\gtrsim 1500$ km s$^{-1}$ — supports a $D^6$ origin for this system. In this context, our detected rotation period could point to LP 398-9 being a $D^6$ donor.

## 4.2 Circumstellar material

LP 398-9 has a strong IR excess that indicates the presence of significant quantities of circumstellar dust. Our optical spectrum shows narrow atomic carbon lines unexplained by the photospheric model, pointing to a circumstellar source of carbon. Our observations suggest a carbon-rich shell of circumstellar material inflated to more than an order of magnitude larger than present-day radius of the star.

The presence of carbon-rich circumstellar material can be plausibly explained by the $D^6$ origin of LP 398-9. The SN Ia explosion of its stellar companion would have significantly polluted the atmosphere of LP 398-9, depositing thermal and radioactive energy and causing the atmosphere (dominated by carbon and oxygen) to puff up. The radius of LP 398-9 inferred from its luminosity and parallax is an order of magnitude larger than that of a typical WD, suggesting that it remains in a somewhat puffed phase like the other two runaways found in Shen et al. (2018b). Mechanical energy from the companion's SN Ia explosion could also have pushed the circumstellar material outwards to larger orbital radii. If some fraction of the inflated layers had detached from the star, it would appear today as an extended carbon-rich circumstellar shell. A low-velocity tail of the SNIa ejecta could also have been retained by LP 398-9 after the explosion. A promising avenue to resolve this question is performing 3-D simulations of the $D^6$ scenario, for example to ascertain the amount and composition of SN ejecta that remain bound to the donor (e.g. Tanikawa et al. 2018).

Under the assumption of an optically thin dust shell surrounding LP 398-9, we can use our observations to approximate the total dust mass. We adopt the fitted black-body dust temperature and Gaia-inferred distance from Table 1. We assume a dust opacity $\kappa(3.4\,\mu\text{m}) = 500$ cm$^2$ g$^{-1}$ (Draine & Lee 1984; Draine 2003; Woitke et al. 2016), consistent with amorphous carbon grains. We estimate the dust mass using the relation from Hildebrand (1983):

$$M_{dust} = \frac{F(\lambda)D^2}{\kappa(\lambda)B(\lambda, T_d)}. \tag{4}$$

Here $B(\lambda, T_d)$ is the Planck function, and $D$ is the parallax-inferred distance. Substituting the *WISE W1* flux as $F(\lambda)$ provides an order-of-magnitude total dust mass $M_{dust} \approx 10^{20}$ g $= 10^{-13}\,M_\odot$. This dust mass is comparable to that of known dust discs around WDs (Jura 2003; Reach et al. 2005), although we stress that LP 398-9's origin and composition is quite different from those systems.

## 5 DISCUSSION

We have presented two new lines of evidence tying LP 398-9 to the $D^6$ SNIa progenitor scenario: circumstellar material and surface rotation. We interpret the 15.4 h photometric signal as a signature of rotationally modulated brightness variations, potentially stemming from surface inhomogeneities left over from the SN explosion $\sim 10^5$ yr ago. The rotational period itself can be explained by angular momentum conservation of LP 398-9 after its companion exploded, assuming the binary was tidally locked at the point of detonation.

Several effects could have altered the rotational rate in the time since the supernova. Since tidal dissipation primarily occurs near the surface of the WD, the surface layers could preferentially synchronize without fully spinning up the core, invalidating our assumption of a rigid-body rotation (e.g. Goldreich & Nicholson 1989; Fuller & Lai 2012a,b, 2014). Additionally, LP 398-9 could have lost angular momentum in the time since the SN explosion. An obvious culprit could be the inflated stellar layers that today present as circumstellar dust tens of stellar radii away. The present-day total dust mass is a minuscule fraction of the stellar mass, making it an unlikely route for angular momentum to leave the system. However, there could have been episodes of further mass loss in the time since the supernova.

Although it is uncertain precisely what processes cause the $D^6$ donor WDs to inflate to their presently observed radii, this inflated phase is probably only temporary (Shen et al. 2018b; Bauer et al. 2019). Due to selection effects, we are most likely to find $D^6$ donors in their inflated state, since these are detectable out to a larger search volume. Our fitted stellar parameters imply a Kelvin-Helmholtz time-scale $\tau_{KH} \gtrsim 20$ Myr for LP 398-9, much longer than the flight time $\approx 0.1$ Myr from the SN remnant G70.0-21.5. As LP 398-9 radiates away energy deposited by tidal heating and the SN itself, it will contract in size and gradually return to the WD cooling track. In the absence of any mechanism to remove angular momentum from the system, its rotation will speed up as it shrinks. Therefore, a plausible long-term outcome of the $D^6$ scenario is a class of rapidly rotating hypervelocity WDs. These might have helium-dominated or carbon-dominated spectral types. However, such hypervelocity systems leave the Galaxy on short time-scale $\lesssim 10$ Myr, making it quite unlikely that we could detect them. Due to these selection effects, we are overwhelmingly likely to find $D^6$ donors in their inflated state.

In ordinary WDs with infrared-emitting discs, the lifetime of dust in the region where it produces infrared excess is limited by Poynting–Robertson drag (Rafikov 2011). However, the Poynting–Robertson time-scale for LP 398-9 is much longer than typical WDs, largely due to its inflated state. Another important effect is sub-micron dust removal via radiation pressure, where the sub-micron dust is created via collisions (Chen, Su & Xu 2020). The collisional lifetime can be high if the infrared excess is produced by a dynamically cold disc with a small internal velocity dispersion, which is nominally consistent with the narrow observed lines of circumstellar carbon (Section 3.4). However, given the poor spectral resolution of our data, this is not a strong constraint. If the collisional lifetime is indeed short, a continuous dust production mechanism could be required to explain the infrared excess $\sim 10^5$ yr after the formation of the system. Ongoing dust production would also account for the IR flux variability we describe in Section 2.1.

When a normal isolated WD has an observed IR excess, the usual explanation is circumstellar dust from a disrupted planetesimal (e.g. Debes & Sigurdsson 2002; Jura 2003; Farihi 2016; Veras 2021). While the existence of disrupted planetesimals around LP 398-9 is tantalizing, it is quite unlikely. The $D^6$ origin of LP 398-9 implies

that it was until recently ($\sim 10^5$ yr ago) in a close binary system with another WD. During the final stages of binary evolution, the two WDs in the theorized $D^6$ scenario would be orbiting too close for a planet to maintain a stable orbit around LP 398-9. While it is plausible that the stars possessed a circumbinary planetary system, any surviving planetesimals must have occupied orbits wide enough to avoid engulfment during giant branch evolution, yet close enough to remain bound to LP 398-9 after the SN Ia of its companion. This scenario can be tested with future infrared spectroscopy — for example with the James Webb Space Telescope (Gardner et al. 2006) — that would reveal the temperature profile, composition, and geometry of the circumstellar material. These observations could also be used to search for thermonuclear ashes deposited by the past supernova.

One question that remains is why LP 398-9 ('D6-2') is the only $D^6$ candidate with an infrared excess, out of the three candidates found by Shen et al. (2018b). 'D6-1' has secure *WISE* data with no detectable IR excess (Fig. 1), while 'D6-3' does not have secure data in *WISE* due to a crowded field. One possible explanation is that the other candidates are the products of older supernovae, and could have consequently lost their circumstellar shell over time. LP 398-9 is the only $D^6$ star with an associated SN remnant, suggesting that it was ejected recently enough that the remnant did not dissipate into the interstellar medium. Conversely, all three $D^6$ stars are clustered closely together on the colour-magnitude diagram and have similar low-resolution spectra, perhaps indicating that they are in similar stages of their evolution. D6-1 and D6-3 should be monitored to search for rotationally modulated variations. If they are indeed the product of older supernovae that LP 398-9, then their surface composition may have homogenized enough to make their rotational signal undetectable. Alternatively, if stark differences persist between LP 398-9 and other $D^6$ donors, then it is important to consider alternative hypotheses for LP 398-9's origin (Bauer et al. 2021; Neunteufel et al. 2021).

Future observations of both LP 398-9 and the other $D^6$ candidates could aid in resolving these questions by placing firmer constraints on the time elapsed since the respective SNe Ia. Further spectroscopic observations of other $D^6$ candidates could search for carbon absorption indicative of circumstellar dust that is too cool to produce an IR excess in *WISE*. Spectroscopy at higher resolution and signal-to-noise across a wide wavelength range could also search for absorption by other elements in the circumstellar material. Additionally, more theoretical modelling could estimate the time-scales over which ejected runaways cool and return to the WD cooling track. Understanding these unique systems will shed light on the mechanism and after-effects of the double-degenerate channel for SNe Ia.

*Software:* NUMPY (Harris et al. 2020), SCIPY (Virtanen et al. 2020), EMCEE (Foreman-Mackey et al. 2013; Foreman-Mackey et al. 2019), MATPLOTLIB (Hunter 2007), LMFIT (Newville & Stensitzki 2018), LTSFIT (Cappellari et al. 2013).

*Facilities:* Gaia, Sloan, WISE, ARC:3.5-m (DIS), GTC:10.4-m (HiPERCAM), Liverpool:2-m (IO:O), INT:2.5-m (WFC), FLWIO:2MASS, HST (STIS), GALEX, IRSA.

## DATA AVAILABILITY

The broadband photometry, *WISE* light curve, ZTF light curve, HiPERCAM light curve, and *HST*-STIS data are all available from respective public data archives. The corresponding author will gladly share any other data products and analysis code upon request.

## REFERENCES

Ahumada R. et al., 2020, ApJS, 249, 3
Bailer-Jones C. A. L., 2015, PASP, 127, 994
Bauer E. B., White C. J., Bildsten L., 2019, ApJ, 887, 68
Bauer E. B., Chandra V., Shen K. J., Hermes J. J., 2021, ApJ, 923, L34
Bellm E. C. et al., 2019, PASP, 131, 1
Benacquista M. J., 2011, ApJ, 740, 3
Bergeron P., Dufour P., Fontaine G., Coutu S., Blouin S., Genest-Beaulieu C., Bédard A., Rolland B., 2019, ApJ, 876, 67
Bildsten L., Shen K. J., Weinberg N. N., Nelemans G., 2007, ApJ, 662, L95
Blanton M. R. et al., 2017, AJ, 154, 28
Bloom J. S. et al., 2012, ApJ, 744, L17
Blouin S., Dufour P., Allard N. F., 2018a, ApJ, 863, 184
Blouin S., Dufour P., Allard N. F., Kilic M., 2018b, ApJ, 867, 161
Brinkworth C. S., Burleigh M. R., Wynn G. A., Marsh T. R., 2004, MNRAS, 348, 33
Brinkworth C. S., Marsh T. R., Morales-Rueda L., Maxted P. F., Burleigh M. R., Good S. A., 2005, MNRAS, 357, 333
Brown A. G. et al., 2021, A&A, 649, 1
Burdge K. B. et al., 2020, ApJ, 905, 32
Cappellari M. et al., 2013, MNRAS, 432, 1709
Chandrasekhar S., 1931, ApJ, 74, 81
Chen C. H., Su K. Y., Xu S., 2020, Nature Astron., 4, 328
Condon J. J., Cotton W. D., Greisen E. W., Yin Q. F., Perley R. A., Taylor G. B., Broderick J. J., 1998, AJ, 115, 1693
Cunningham T. et al., 2021, MNRAS, 503, 1646
Cutri R. M. et al., 2012, Explanatory Supplement to the WISE All-Sky Data Release Products. https://wise2.ipac.caltech.edu/docs/release/allsky/expsup/index.html
Dan M., Rosswog S., Guillochon J., Ramirez-Ruiz E., 2011, ApJ, 737, 89
Debes J. H., Sigurdsson S., 2002, ApJ, 572, 556
Dennihy E., Farihi J., Fusillo N. P. G., Debes J. H., 2020, ApJ, 891, 97
de los Reyes M. A. C., Kirby E. N., Seitenzahl I. R., Shen K. J., 2020, ApJ, 891, 85
Dhawan S., Leibundgut B., Spyromilio J., Blondin S., 2017, A&A, 602, A118
Dhillon V. S. et al., 2016, in Evans C. J., Simard L., Takami H., eds, Proc. SPIE Conf. Ser. Vol. 9908, Ground-based and Airborne Instrumentation for Astronomy VI. SPIE, Bellingham, p. 99080Y

Dhillon V. et al., 2018, in Evans C. J., Simard L., Takami H., eds, Proc. SPIE Conf. Ser. Vol. 10702, Ground-based and Airborne Instrumentation for Astronomy VII. SPIE, Bellingham, p. 107020L

Dhillon V. S. et al., 2021, MNRAS, 507, 350

Doi M. et al., 2010, AJ, 139, 1628

Draine B. T., 2003, ARA&A, 41, 241

Draine B. T., 2011, Physics of the Interstellar and Intergalactic Medium. Princeton Univ. Press, Princeton

Draine B. T., Lee H. M., 1984, ApJ, 285, 89

Farihi J., 2016, New Astron. Rev., 71, 9

Ferrario L., Vennes S., Wickramasinghe D. T., Bailey J. A., Christian D. J., 1997, MNRAS, 292, 205

Fesen R. A., Neustadt J. M., Black C. S., Koeppel A. H., 2015, ApJ, 812, 37

Fitzpatrick E. L., Massa D., 2007, ApJ, 663, 320

Foreman-Mackey D., Hogg D. W., Lang D., Goodman J., 2013, PASP, 125, 306

Foreman-Mackey D. et al., 2019, J. Open Source Softw., 4, 1864

Fukugita M., Ichikawa T., Gunn J. E., Doi M., Shimasaku K., Schneider D. P., 1996, AJ, 111, 1748

Fuller J., Lai D., 2011, MNRAS, 412, 1331

Fuller J., Lai D., 2012a, ApJ, 756, 2

Fuller J., Lai D., 2012b, MNRAS, 421, 426

Fuller J., Lai D., 2014, MNRAS, 444, 3488

Gaia Collaboration et al., 2021, A&A, 649, 1

Gänsicke B. T., Rodríguez-Gil P., Gentile Fusillo N. P., Inight K., Schreiber M. R., Pala A. F., Tremblay P. E., 2020, MNRAS, 499, 2564

Gardner J. P. et al., 2006, SSRv, 123, 485

Goldreich P., Nicholson P. D., 1989, ApJ, 342, 1079

Green G., 2018, J. Open Source Softw., 3, 695

Green G. M. et al., 2015, ApJ, 810, 25

Green G. M. et al., 2018a, MNRAS, 478, 651

Green M. J. et al., 2018b, MNRAS, 477, 5646

Guidry J. A. et al., 2021, ApJ, 912, 125

Guillochon J., Dan M., Ramirez-Ruiz E., Rosswog S., 2010, ApJ, 709, L64

Gunn J. E. et al., 1998, AJ, 116, 3040

Harris C. R. et al., 2020, Nature, 585, 357

Hasegawa T. I., Kwok S., 2003, ApJ, 585, 475

Hermes J. J., Putterman O., Hollands M. A., Wilson D. J., Swan A., Raddi R., Shen K. J., Gänsicke B. T., 2021, ApJ, 914, L3

Hibbert A., Biemont E., Godefroid M., Vaeck N., 1993, A&AS, 99, 179

Hildebrand R. H., 1983, QJRAS, 24, 267

Hillebrandt W., Niemeyer J. C., 2000, ARA&A, 38, 191

Hunter J. D., 2007, Comput. Sci. Eng., 9, 90

Iben I. J., Tutukov A. V., 1984, ApJS, 54, 335

Iben I., Jr., Tutukov A. V., Fedorova A. V., 1998, ApJ, 503, 344

Johansson L., 1966, Ark. Fys. (Stockholm), 31, 201

Johnson R. C., 1927, RSPTA, 226, 157

Jura M., 2003, ApJ, 584, L91

Kasen D., 2010, ApJ, 708, 1025

Keene J., Young K., Phillips T. G., Buettgenbach T. H., Carlstrom J. E., 1993, ApJ, 415, L131

Kenyon S. J., Bromley B. C., 2017a, ApJ, 844, 116

Kenyon S. J., Bromley B. C., 2017b, ApJ, 850, 50

Kerzendorf W. E., Schmidt B. P., Asplund M., Nomoto K., Podsiadlowski P., Frebel A., Fesen R. A., Yong D., 2009, ApJ, 701, 1665

Kilic M. et al., 2015, ApJ, 814, L31

Kirby E. N. et al., 2019, ApJ, 881, 45

Kramida A., Ralchenko Yu., Reader J., and NIST ASD Team, 2021, NIST Atomic Spectra Database (ver. 5.9). National Institute of Standards and Technology, Gaithersburg, MD [Online]. Available: https://physics.nist.gov/asd [2022, January 19]

Li W. et al., 2011, Nature, 480, 348

Lindegren L. et al., 2021, A&A, 649, A2

Lindegren L. et al., 2021, A&A, 649, A4

Lomb N. R., 1976, Ap&SS, 39, 447

Luo D., Pradhan A. K., 1989, J. Phys. B, 22, 3377

Mainzer A. et al., 2011, ApJ, 731, 53

Mainzer A. et al., 2014, ApJ, 792, 30

Maoz D., Mannucci F., Nelemans G., 2014, ARA&A, 52, 107

Maoz D., Mazeh T., McQuillan A., 2015, MNRAS, 447, 1749

Margutti R. et al., 2012, ApJ, 751, 134

Martin D. C. et al., 2005, ApJ, 619, L1

Masci F. J. et al., 2019, PASP, 131, 1

Matteucci F., Spitoni E., Recchi S., Valiante R., 2009, A&A, 501, 531

Mignard F. et al., 2018, A&A, 616, A14

Million C. et al., 2016, ApJ, 833, 292

Neunteufel P., Preece H., Kruckow M., Geier S., Hamers A. S., Justham S., Podsiadlowski P., 2021, A&A, http://arxiv.org/abs/2112.07469

Newville M., Stensitzki T., 2018, Non-Linear Least-Squares Minimization and Curve-Fitting for Python

Nomoto K., 1982, ApJ, 253, 798

Pakmor R., Kromer M., Taubenberger S., Springel V., 2013, ApJ, 770, 7

Pelisoli I. et al., 2021, MNRAS, 5, 1

Perlmutter S. et al., 1999, ApJ, 517, 565

Piro A. L., 2011, ApJ, 740, 2

Prusti T. et al., 2016, A&A, 595, 36

Raddi R., Hollands M. A., Gänsicke B. T., Townsley D. M., Hermes J. J., Gentile Fusillo N. P., Koester D., 2018a, MNRAS, 479, L96

Raddi R., Hollands M. A., Koester D., Gänsicke B. T., Fusillo N. P. G., Hermes J. J., Townsley D. M., 2018b, ApJ, 858, 3

Raddi R. et al., 2019, MNRAS, 489, 1489

Rafikov R. R., 2011, ApJ, 732, L3

Rafikov R. R., Garmilla J. A., 2012, ApJ, 760, 123

Raskin C., Scannapieco E., Fryer C., Rockefeller G., Timmes F. X., 2012, ApJ, 746, 62

Raymond J. C., Caldwell N., Fesen R. A., Weil K. E., Boumis P., di Cicco D., Mittelman D., Walker S., 2020, ApJ, 888, 90

Reach W. T., Kuchner M. J., von Hippel T., Burrows A., Mullally F., Kilic M., Winget D. E., 2005, ApJ, 635, L161

Reding J. S., Hermes J. J., Vanderbosch Z., Dennihy E., Kaiser B. C., Mace C. B., Dunlap B. H., Clemens J. C., 2020, ApJ, 894, 19

Riess A. G. et al., 1998, AJ, 116, 1009

Riess A. G., Casertano S., Yuan W., Macri L. M., Scolnic D., 2019, ApJ, 876, 85

Rousseeuw P. J., Van Driessen K., 2006, Data Min. and Knowl. Discovery, 12, 29

Sanders J. L., Belokurov V., Man K. T., 2021, MNRAS, 506, 4321

Scalzo R. et al., 2014, MNRAS, 440, 1498

Scargle J. D., 1982, ApJ, 263, 835

Shen K. J., 2015, ApJ, 805, 1

Shen K. J., Bildsten L., 2014, ApJ, 785, 9

Shen K. J., Schwab J., 2017, ApJ, 834, 180

Shen K. J., Kasen D., Miles B. J., Townsley D. M., 2018a, ApJ, 854, 52

Shen K. J. et al., 2018b, ApJ, 865, 15

Shen K. J., Blondin S., Kasen D., Dessart L., Townsley D. M., Boos S., Hillier D. J., 2021a, ApJ, 909, L18

Shen K. J., Boos S. J., Townsley D. M., Kasen D., 2021b, ApJ, 922, 68

Skrutskie M. F. et al., 2006, AJ, 131, 1163

Soker N., 2019, New Astron. Rev., 87, 101535

Sorahana S., Yamamura I., Murakami H., 2013, ApJ, 767, 77

Steele I. A. et al., 2004, in Oschmann J. M., Jr, ed., Proc. SPIE Conf. Ser. Vol. 5489, Ground-based Telescopes. SPIE, Bellingham, p. 679

Swan W., 1857, Trans. R. Soc. Edinburgh, 21, 411

Swan A., Farihi J., Wilson T. G., 2019, MNRAS, 484, L109

Swan A., Farihi J., Wilson T. G., Parsons S. G., 2020, MNRAS, 496, 5233

Swan A., Kenyon S. J., Farihi J., Dennihy E., Gänsicke B. T., Hermes J. J., Melis C., von Hippel T., 2021, MNRAS, 506, 432

Taam R. E., 1980, ApJ, 237, 142

Tanikawa A., Nomoto K., Nakasato N., 2018, ApJ, 868, 90

Tanikawa A., Nomoto K., Nakasato N., Maeda K., 2019, ApJ, 885, 103

Tinsley B. M., 1979, ApJ, 229, 1046

Tody D., 1986, in Crawford D. L., ed., Proc. SPIE Conf. Ser. Vol. 627, Instrumentation in astronomy VI. SPIE, Bellingham, p. 733

Tremblay P. E., Fontaine G., Freytag B., Steiner O., Ludwig H. G., Steffen M., Wedemeyer S., Brassard P., 2015, ApJ, 812, 19

Vennes S., Nemeth P., Kawka A., Thorstensen J. R., Khalack V., Ferrario L., Alper E. H., 2017, Science, 357, 680

Veras D., 2021, Planetary Systems Around White Dwarfs. Oxford Univ. Press, Oxford, p. 1

Virtanen P. et al., 2020, Nature Methods, 17, 261

von Hippel T., Kuchner M. J., Kilic M., Mullally F., Reach W. T., 2007, ApJ, 662, 544

Webbink R. F., 1984, ApJ, 277, 355

Whelan J., Iben, Icko J., 1973, ApJ, 186, 1007

Woitke P. et al., 2016, A&A, 586, A103

Woodgate B. E. et al., 1998, PASP, 110, 1183

Woods T. E., Ghavamian P., Badenes C., Gilfanov M., 2017, NatAs, 1, 800

Wright E. L. et al., 2010, AJ, 140, 1868

Xu S. et al., 2018, MNRAS, 474, 4795

Yu H., Weinberg N. N., Fuller J., 2020, MNRAS, 496, 5482

Yu H., Fuller J., Burdge K. B., 2021, MNRAS, 501, 1836

This paper has been typeset from a TeX/LaTeX file prepared by the author.